McPhillimy, J., May, S., Klitis, C., Guilhabert, B., Dawson, M. D., Sorel, M. and Strain, M. J. (2020) Transfer printing of AlGaAs-on-SOI microdisk resonators for selective mode coupling and low-power nonlinear processes. Optics Letters, 45(4), pp. 881-884.

http://eprints.gla.ac.uk/213145/

Deposited on: 2 April 2020

Transfer printing of AlGaAs-on-SOI micro-disk resonators for selective mode coupling and low-power non-linear processes

JOHN MCPHILLIMY[1], STUART MAY[2], CHARALAMBOS KLITIS[2], BENOIT GUILHABERT[1], MARTIN D. DAWSON[1], MARC SOREL[2], AND MICHAEL J. STRAIN[1,*]

[1]Institute of Photonics, Dept. of Physics, University of Strathclyde, Glasgow G1 1RD, UK
[2]School of Engineering, University of Glasgow, Glasgow, Oakfield Avenue, Glasgow, G12 8LT, UK
*Corresponding author: michael.strain@strath.ac.uk

The transfer printing of aluminium gallium arsenide (AlGaAs) micro-disk resonators onto a silicon-on-insulator (SOI) waveguide platform is demonstrated. The integrated resonators exhibit loaded Q-factors reaching 4×10^4, and the vertical assembly approach allows selective coupling to different spatial mode families. The hybrid platform's non-linearity is characterized by four-wave mixing (FWM) with a measured non-linear coefficient of γ=325 (Wm)$^{-1}$, with the devices demonstrating minimal two-photon absorption (TPA) and free-carrier absorption (FCA) losses that are inherent to SOI at telecommunications wavelengths.

Non-linear optical phenomena have been employed in a wide range of applications in integrated photonics, from all-optical switching [1] and frequency conversion [2], to photon pair generation [3]. Chip-scale non-linear photonics benefits from the high optical confinement of waveguide and resonator devices and the possibility of integrating multiple components together in complex systems [4]. The large number of optical material platforms available has led to demonstrations spanning III-Vs [5], diamond [6], dielectrics [7] and silicon [8], amongst others.

Silicon has been widely taken up as a platform for large scale photonic integrated circuits (PICs) due to its low propagation losses at telecommunications wavelengths, high confinement waveguides, and the potential for volume manufacturing in electronics foundries. Nevertheless, there are a number of limitations silicon presents as a non-linear optical material, including a lack of $\chi^{(2)}$ non-linearity. Importantly, at telecommunications wavelengths it presents significant two-photon and related free carrier losses, limiting power scaling of $\chi^{(3)}$ parametric process for even moderate pump levels [8].

Alternatively, AlGaAs materials have significant $\chi^{(2)}$ and $\chi^{(3)}$ non-linearities, and when operated around 1.55 μm, are far enough from the half-bandgap to avoid significant TPA effects

[9]. High performance AlGaAs non-linear waveguide devices are well-established, but have thus far not been integrated into photonic integrated circuits of significant complexity. Recent advances in wafer and die bonding techniques have allowed the demonstration of AlGaAs-on-insulator (AlGaAs-o-I) devices that overcome previous constraints on device geometries imposed by low index contrast AlGaAs on GaAs/AlGaAs wafer designs [10], allowing for dispersion engineering and demonstration of high efficiency non-linear processes [11].

In this work we present a hybrid integration scheme to make use of the potential for complex PIC fabrication in silicon, with the efficient non-linear performance of AlGaAs materials on a single chip. AlGaAs micro-photonic devices are fabricated separately from the silicon chips and integrated in a post-process micro-assembly technique known as transfer printing (TP) [12]. The vertical integration scheme allows direct optical coupling between single-mode silicon waveguides and devices fabricated in complementary materials, as shown previously with the integration of nanolasers and single-photon sources onto silicon [13, 14]. The TP method presented here has previously demonstrated sub-micron accuracy for the hybrid integration of laterally [15] and vertically coupled [16] resonator devices, using automated optical microscope alignment by a computer aided marker registration procedure. This enables the direct integration of AlGaAs micro-disk resonators onto silicon waveguide circuits, where control over the relative horizontal and vertical position of the disk with respect to the silicon bus waveguide provides control over the coupling fraction to multiple disk spatial modes, something that is challenging for devices fabricated in a single material layer. The high level of lateral and vertical coupling control provided by transfer printing provides an effective route towards efficient 3D integrated photonic systems. Disk resonators are fabricated with loaded Q-factors reaching 4×10^4 and losses in the range of $\approx$1.95 dB/cm, demonstrating the accuracy of the device printing process without introducing significant propagation losses in transferred devices. Finally, four-wave mixing is demonstrated in the AlGaAs disk with an efficiency commensurate with the device modal area and material non-linear refractive index.

The fabrication procedure is shown in figure 1. The III-V wafer is composed of an Al$_x$Ga$_{1-x}$As epitaxial stack with a 270
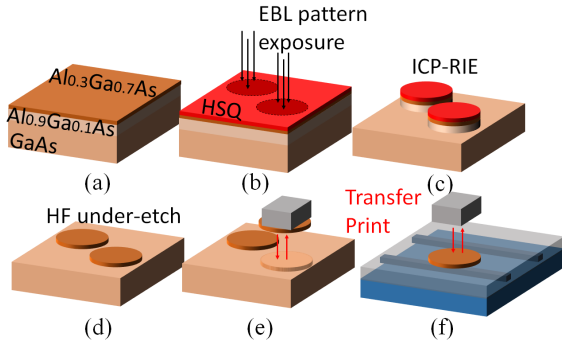
Fig. 1. Schematic of AlGaAs micro-disk fabrication showing (a) initial AlGaAs/GaAs wafer material stack; (b) microdisk patterning into HSQ resist followed by a full etch of the $Al_{0.3}Ga_{0.7}As$ and $Al_{0.9}Ga_{0.1}As$ layers by an ICP-RIE process; (c) under-etch of core layer by removing $Al_{0.9}Ga_{0.1}As$ sacrificial material by a buffered (10:1) HF wet etch; (d) TP to nonnative SOI receiver.

nm thick $Al_{0.3}Ga_{0.7}As$ core layer and a 0.5 μm-thick $Al_{0.9}Ga_{0.1}As$ sacrificial layer, grown by molecular-beam epitaxy onto a GaAs substrate. The control over each layer's aluminium content allows selective layer etching. The etch mask for the micro-disks is patterned using electron-beam lithography (EBL) into a hydrogen silsequioxane (HSQ) hard mask. This pattern is transferred to the core ($Al_{0.3}Ga_{0.7}As$) and sacrificial ($Al_{0.9}Ga_{0.1}As$) layers using a $SiCl_4/Ar/N_2$ inductively-coupled plasma reactive ion etch (ICP-RIE) recipe. A buffered hydrofluoric acid (HF) 10:1 wet etch is then used to selectively remove the exposed sacrificial $Al_{0.9}Ga_{0.1}As$ layer. After wet etching of the sacrificial layer, the AlGaAs disks are fully released onto the GaAs substrate, and can be displaced from their lithographically defined positions by $\approx20\mu$m. This allows identification of individual devices by relative position to non-underetched marker features. An SOI photonic chip is used as the receiving platform. This is composed of a 220 nm silicon core layer and 2 μm buried oxide. Single-mode waveguides of 500 nm width are fabricated using e-beam lithography into HSQ resist, followed by an ICP-RIE SF_6/C_4F_8 recipe [17]. Finally, an HSQ uppercladding of 250nm is deposited and thermally cured at 180°C to produce a planarised chip surface.

The TP procedure is illustrated in figure 1e-f, using the reversible adhesion model [18]. A polydimethylsiloxane (PDMS) stamp is used for the printing, and is composed of a $100\times100\mu$m body with a single, centrally located, pyramidal feature of 12μm width and 8.5μm height. The simple stamp design allows the transfer printing of a wide range of different sized disk devices. The adhesion of the PDMS stamp to the disk readily overcomes the adhesion of the disk to the exposed GaAs substrate when using a reversible adhesion method with the relative velocity of the pick-up and release process as a parameter [18]. Furthermore, the TP can be achieved without any adhesion promoting layers due to the low interface roughness. AFM measurements of the HSQ cladding layer and AlGaAs disk underside exhibit r.m.s roughness values of below 1 nm.

Figure 2a shows a schematic of the final micro-assembled device. The HSQ uppercladding provides a vertical coupling offset of Δy=250 nm between silicon waveguide and micro-disk, and the edge-to-edge lateral offset, Δx, is controlled by the transfer printing. An optical microscope image of a fully assembled AlGaAs micro-disk resonator printed onto a silicon waveguide
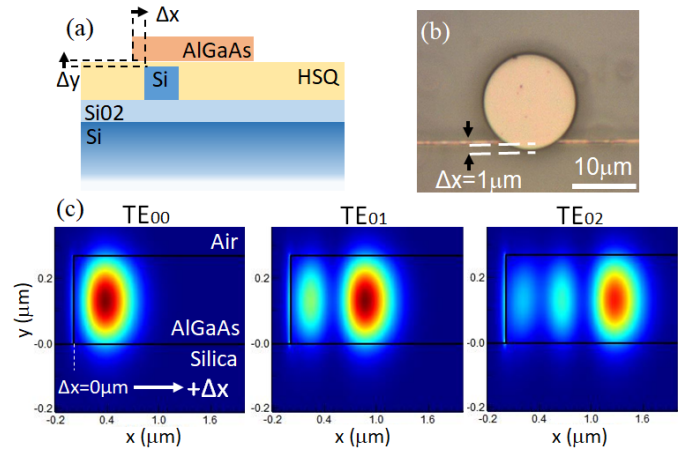

Fig. 2. (a) Schematic of the micro-disk resonator, showing lateral and vertical offsets. (b) Optical image of an AlGaAs-on-SOI disk assembled by transfer printing. (c) Cross-section of simulated TE modes distributed within the micro-disk resonator cavity, showing the mode intensity distributions in the disk cavity and the bus waveguide lateral offset positions (Δx). The computed mode profiles are calculated for isolated AlGaAs disks on a silica substrate with an air cladding.

is shown in figure 2b. Micro-disk cavities are highly multimode structures, with the lack of lateral confinement supporting higher order radial modes. Figure 2c shows simulated mode profiles of the first three radial TE modes of the micro-disk. Simulations were performed using a finite-difference eigenmode (FDE) solver. For each mode order the effective index, group index and effective modal area (A_{eff}) were calculated as a function of wavelength. The modal coupling between the silicon bus waveguide and the disk modes is dependent on the their relative effective indices and modal area overlaps. For example, a lateral offset of Δx$\leqslant$500nm shows a peak mode overlap with the disk TE_{00} mode. As Δx increases beyond 500nm the maximum mode overlap corresponds to the TE_{01} mode, finally shifting towards the TE_{02} mode as Δx reaches 1000nm.

A measured transmission spectrum of a fabricated device with Δx = 500 nm is presented in figure 3a. The characteristics of each individual resonance are extracted using a non-linear least squares fit to a theoretical model of an all-pass resonator, leaving
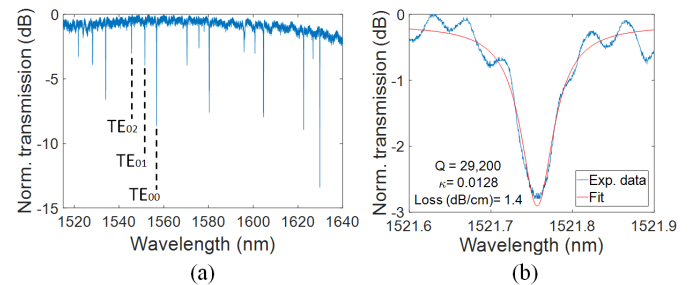
Fig. 3. (a) Normalised transmission spectrum of the hybrid resonator showing multimode coupling. The AlGaAs micro-disk has a radius of 5μm with a lateral offset of Δx=500 nm (b) Analytic fitting of a single resonance including the measured loaded Q-factor, cross-coupling coefficient (κ) and distributed propagation loss values.
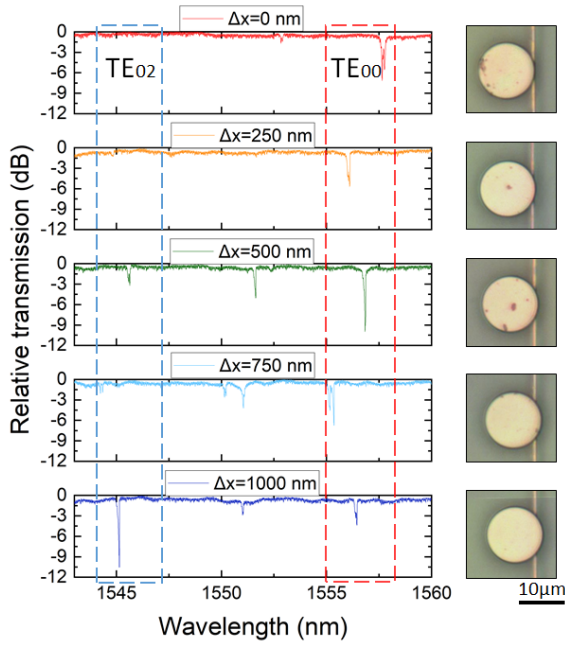
Fig. 4. Transmission spectra of AlGaAs-SOI micro-disk resonators with varying lateral separation (Δx) from 0 nm to 1 μm in steps of 250 nm, top to bottom respectively. The resonant mode coupling power shift from fundamental TE$_{00}$ to a higher order TE$_{02}$ is evident when increasing Δx.

coupling coefficient (κ) and distributed loss as free parameters [19]. A single resonance fit is shown in figure 3b with a loaded Q-factor of 2.9×10^4 (intrinsic Q-factor of 2×10^5), $\kappa = 0.0128$ and distributed loss of 1.4 dB/cm. It is clear from figure 3 that the device exhibits a number of resonant modes. Assignment of the resonant peaks to each optical TE mode can be achieved by comparing simulated and experimental free spectral ranges (FSR). The simulated FSR is calculated by FSR=$(\lambda_R^2)/(n_g \cdot L_c)$, where the group index (n_g) can be calculated from the mode simulations, L_c is the cavity length, and λ_R is the resonance wavelength. Simulated FSRs were calculated as FSR=23.7, 24.6, and 25.3 nm for TE$_{00}$, TE$_{01}$, and TE$_{02}$, respectively. Experimental FSRs are extracted from the three distinct optical modes families in figure 3, with FSR = 24, 24.6, and 25.2 nm measured. The experimental values match the simulated results well, with the relevant optical mode resonances identified in figure 3.

By using high accuracy TP, the production of vertically coupled AlGaAs-SOI micro-disk resonators with selective mode coupling can be achieved, for a fixed value of Δy, through variation of Δx. Multiple hybrid resonator devices were assembled with varying lateral separations varying from Δx=0 μm to Δx=1 μm in steps of 250 nm, as shown in figure 4.

The corresponding transmission spectra were measured for each device, with the variation of mode coupling between two optical modes (TE$_{00}$ and TE$_{02}$) highlighted as a function of Δx around a centre wavelength of $\lambda \approx$1550 nm. By gradually increasing the lateral coupling offset, the overlap position of the silicon waveguide moves further towards the inward regions of the disk cavity. As this occurs, the coupling to the fundamental mode (red dotted region) is reduced. A large enough positional overlap between the disk and waveguide causes an inversion in the coupling ratio between the mode families, with the higher order mode becoming more visible for a lateral offset of Δx=1000

Table 1. Selective mode coupling: Q-factor and κ.

	TE$_{00}$		
Δx	Loaded Q-factor	Intrinsic Q-factor	κ
0	2.1×10^4	8.9×10^4	0.0108
250	2.8×10^4	1.4×10^5	0.0091
500	2.9×10^4	1.2×10^5	0.0084
750	3.8×10^4	4.8×10^4	0.0081
	TE$_{02}$		
1000	3.0×10^4	1.1×10^5	0.0075

nm (blue dotted region). The variation in absolute resonant wavelengths between different devices can be attributed to fabrication tolerances on the disk diameter that may be in the order of 1.5 nm [17], leading to potential shifts in the resonance position in the order of 2nm. The change in Q-factor and κ values across the range of micro-assembled devices are provided in table 1, showing the gradual variation in coupling across both modes for a changing Δx. Values for the Q-factor are not presented in cases where there is significant resonance mode-splitting, for example for TE$_{00}$ (Δx=1000 nm) and TE$_{02}$ (Δx=500,750 nm). Surface contamination due to redeposition of material released during the under-etch process is visible on several micro-disks, as shown in the top-view optical images in figure 4. This can cause slight increases in the overall distributed losses, with an increased round-trip loss of 0.06dB for the worst case scenario (Δx=0 nm), however this effect is not significantly larger than fabrication loss variations dominated by sidewall roughness scattering.

The FWM efficiency (η) of integrated micro-resonator devices depends on the material non-linearity, n$_2$, the effective area of the optical mode, A$_{eff}$, linear and non-linear losses and the waveguide dispersion, as detailed in [20]:

$$\eta \equiv \frac{P_i}{P_s} = |\gamma P_p L_{eff}|^2 F_p^2 F_s F_i$$

$$L_{eff}^2 = L^2 exp(-\alpha L) \left| \frac{1 - exp(-\alpha L + j\Delta kL)}{\alpha L - j\Delta kL} \right|^2$$

$$F_{p,s,i} = \left| \frac{r}{1 - texp(-\frac{\alpha L}{2}) + jk_{p,s,i}L} \right|^2,$$

where L and L$_{eff}$ are the cavity geometric and effective lengths, respectively, F$_{p,s,i}$ is the square of the field enhancement factor for the pump, signal, or idler beams. α is the average field propagation loss coefficient incorporating both TPA and FCA losses, k$_{p,s,i}$ are the wavenumbers associated with the pump, idler, and signal beams, respectively, r and t are the cross-coupling and transmission coefficients of the resonator-bus waveguide coupler. γ is the effective non-linearity, where γ = $(2\pi$ n$_2)/(\lambda$ A$_{eff})$ [21] and λ is the resonant wavelength. Therefore, the micro-resonator with a lateral offset of Δx= 750 nm, was selected for FWM experiments, due to the high Q-factor of its fundamental mode set which presents the minimum effective area for the mode families supported in the disk, A$_{eff}$ =0.25 μm^2, calculated from the FDE mode solutions. γ for the fundamental mode can be calculated from the material non-linear index and effective modal area as γ= 325 (Wm)$^{-1}$. Finally, the FDE mode solutions
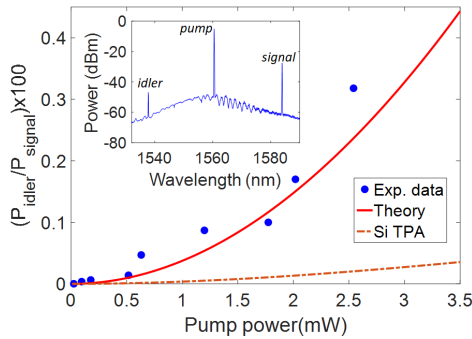
Fig. 5. FWM efficiency ratio as a function of on-chip pump power for a 5 μm-radius AlGaAs-SOI micro-disk resonator. The blue dots and red curve depict the experimental data and theoretical efficiency. The orange dashed curve represents the theoretical efficiency for a silicon resonator of identical geometry exhibiting TPA and FCA losses. Inset shows the FWM spectra for an output pump power of $\approx$0.3 mW with labelled on-resonance pump, signal and idler peaks.

allow calculation of the expected modal dispersion that is incorporated in the model as the phase mismatch of the wavenumbers for each wavelength, given by $\Delta k = 2k_p - k_s - k_i$.

The devices calculated power dependent FWM efficiency is plotted as the red curve in figure 5. The dashed curve in figure 5 corresponds to the calculated efficiency for a silicon resonator with geometry, coupling coefficient, dispersion, and distributed losses identical to the AlGaAs-on-SOI micro-disk resonator. This allows a direct comparison of the silicon and hybrid AlGaAs-on-SOI platforms based solely on variations in their material non-linearity, with a non-linear index $n_2 = 6.5 \times 10^{-18}$m^{2}W^{-1}, TPA of 0.7 cm/GW, and FCA lifetime of 500 ps implemented for silicon [20]. A decreased FWM efficiency for silicon is shown compared to the AlGaAs-on-SOI curve. This can be attributed to silicon's lower n_2, and the effects of TPA and FCA causing significant reductions in the efficiency for higher on-chip powers.

The experimental setup used for the FWM measurements is previously described in [22]. The FWM efficiency is defined as the idler-to-signal ratio (P_i / P_s), as a function of the on-chip pump power (P_p) with the experimental FWM spectra of pump, signal, and idler peaks plotted in figure 5. Both the P_p and P_s values are measured in off-resonance conditions. The pump and signal wavelengths are then tuned on-resonance to the cavity to generate the measured idler. The measured FWM efficiency as a function of P_p is shown in figure 5 as blue dots. There is clear agreement between the measured data and the calculated efficiency curve, both exhibiting a quadratic relationship between injected pump power and FWM efficiency. A maximum experimental efficiency η=-24.9 dB at P_p=2.5 mW is achieved.

The current state-of-the-art in AlGaAs micro-resonators have a calculated non-linear coefficient of γ=630 (Wm)$^{-1}$, with an experimentally achieved FWM conversion efficiency of η=-12 dB at P_p= 7 mW [11]. The lower efficiencies demonstrated in this work follow the theoretical predictions well, giving confidence that the limitation is due to modal area and dispersion effects, rather than limitations introduced by the integration method. By optimizing the device geometry to limit dispersion and $\Delta\lambda$, which can be achieved by implementing single-mode conditions and increasing cavity length, greater phase matching can be designed, enabling improved FWM for future devices.

In conclusion, the vertical integration of AlGaAs-on-SOI

micro-disk resonators has been demonstrated by transfer printing. The hybrid resonators exhibit loaded Q-factors reaching 4×10^4 and losses in the range of $\approx$1.95 dB/cm, showing the ability to selectively couple into different spatial modes. The non-linear capability of the hybrid platform is demonstrated, with a non-linear coefficient calculated as γ=325 (Wm)$^{-1}$, with a FWM efficiency of η=-24.9 dB at an on-chip pump power of 2.5 mW. The hybrid resonators do not exhibit silicon's non-linear TPA and FCA losses, providing a promising method to produce a full suite of non-linear processes on the SOI platform.

The corresponding dataset can be found at DOI: 10.15129/5b546db9-48dc-4069-9961-031fe5f0d87a.

Disclosures. The authors declare no conflicts of interest.

REFERENCES

1. C. Lacava, M. J. Strain, P. Minzioni, I. Cristiani, and M. Sorel, "Integrated nonlinear mach zehnder for 40 gbit/s all-optical switching," Opt. Express **21**, 21587 (2013).
2. S. May, M. Kues, M. Clerici, and M. Sorel, "Second-harmonic generation in AlGaAs-on-insulator waveguides," Opt. Lett. **44**, 1339 (2019).
3. Y. Guo, W. Zhang, S. Dong, Y. Huang, and J. Peng, "Telecom-band degenerate-frequency photon pair generation in silicon microring cavities," Opt. Lett. **39**, 2526 (2014).
4. N. C. Harris, D. Grassani, A. Simbula, M. Pant, M. Galli, T. Baehr-Jones, M. Hochberg, D. Englund, D. Bajoni, and C. Galland, "Integrated source of spectrally filtered correlated photons for large-scale quantum photonic systems," Phys. Rev. X **4** (2014).
5. G. Stegeman, A. Villeneuve, and J. Kang, "Algaas below half bandgap: The silicon of nonlinear optical materials," J. Nonlinear Opt. Phys. & Mater. **03**, 347–371 (1994).
6. B. J. M. Hausmann, I. Bulu, V. Venkataraman, P. Deotare, and M. Lončar, "Diamond nonlinear photonics," Nat. Photonics **8**, 369–374 (2014).
7. M. Ferrera, L. Razzari, D. Duchesne, R. Morandotti, Z. Yang, M. Liscidini, J. E. Sipe, S. Chu, B. E. Little, and D. J. Moss, "Low-power continuous-wave nonlinear optics in doped silica glass integrated waveguide structures," Nat. Photonics **2**, 737–740 (2008).
8. H. K. Tsang and Y. Liu, "Nonlinear optical properties of silicon waveguides," Semicond. Sci. Technol. **23**, 064007 (2008).
9. J. Aitchison, D. Hutchings, J. Kang, G. Stegeman, and A. Villeneuve, "The nonlinear optical properties of AlGaAs at the half band gap," IEEE J. Quantum Electron. **33**, 341–348 (1997).
10. J. J. Wathen, P. Apiratikul, C. J. K. Richardson, G. A. Porkolab, G. M. Carter, and T. E. Murphy, "Efficient continuous-wave four-wave mixing in bandgap-engineered AlGaAs waveguides," Opt. Lett. **39**, 3161 (2014).
11. M. Pu, H. Hu, L. Ottaviano, E. Semenova, D. Vukovic, L. K. Oxenløwe, and K. Yvind, "Ultra-efficient and broadband nonlinear AlGaAs-on-insulator chip for low-power optical signal processing," Laser & Photonics Rev. **12**, 1800111 (2018).
12. B. Corbett, R. Loi, W. Zhou, D. Liu, and Z. Ma, "Transfer print techniques for heterogeneous integration of photonic components," Prog. Quantum Electron. **52**, 1–17 (2017).
13. J. Lee, I. Karnadi, J. T. Kim, Y.-H. Lee, and M.-K. Kim, "Printed nanolaser on silicon," ACS Photonics **4**, 2117–2123 (2017).
14. R. Katsumi, Y. Ota, M. Kakuda, S. Iwamoto, and Y. Arakawa, "Transfer-printed single-photon sources coupled to wire waveguides," Optica **5**, 691 (2018).
15. B. Guilhabert, J. McPhillimy, S. May, C. Klitis, M. D. Dawson, M. Sorel, and M. J. Strain, "Hybrid integration of an evanescently coupled AlGaAs

microdisk resonator with a silicon waveguide by nanoscale-accuracy transfer printing," Opt. Lett. **43**, 4883 (2018).

16. J. McPhillimy, B. Guilhabert, C. Klitis, M. D. Dawson, M. Sorel, and M. J. Strain, "High accuracy transfer printing of single-mode membrane silicon photonic devices," Opt. Express **26**, 16679 (2018).

17. M. Gnan, S. Thoms, D. Macintyre, R. D. L. Rue, and M. Sorel, "Fabrication of low-loss photonic wires in silicon-on-insulator using hydrogen silsesquioxane electron-beam resist," Electron. Lett. **44**, 115 (2008).

18. J. Wu, S. Kim, W. Chen, A. Carlson, K.-C. Hwang, Y. Huang, and J. A. Rogers, "Mechanics of reversible adhesion," Soft Matter **7**, 8657 (2011).

19. W. Bogaerts, P. D. Heyn, T. V. Vaerenbergh, K. D. Vos, S. K. Selvaraja, T. Claes, P. Dumon, P. Bienstman, D. V. Thourhout, and R. Baets, "Silicon microring resonators," Laser & Photonics Rev. **6**, 47–73 (2011).

20. A. C. Turner, M. A. Foster, A. L. Gaeta, and M. Lipson, "Ultra-low power parametric frequency conversion in a silicon microring resonator," Opt. Express **16**, 4881 (2008).

21. J. Leuthold, C. Koos, and W. Freude, "Nonlinear silicon photonics," Nat. Photonics **4**, 535–544 (2010).

22. M. J. Strain, C. Lacava, L. Meriggi, I. Cristiani, and M. Sorel, "Tunable q-factor silicon microring resonators for ultra-low power parametric processes," Opt. Lett. **40**, 1274 (2015).